Self-alignment of a compact large-area atomic Sagnac interferometer

2012 New J. Phys. 14 015002

(http://iopscience.iop.org/1367-2630/14/1/015002)

New Journal of Physics
The open-access journal for physics

Self-alignment of a compact large-area atomic Sagnac interferometer

G Tackmann[1], P Berg, C Schubert, S Abend, M Gilowski, W Ertmer and E M Rasel

Institut für Quantenoptik, Leibniz Universität Hannover, Welfengarten 1, 30167 Hannover, Germany
E-mail: tackmann@iqo.uni-hannover.de

New Journal of Physics **14** (2012) 015002 (14pp)
Received 11 July 2011
Published 20 January 2012
Online at http://www.njp.org/
doi:10.1088/1367-2630/14/1/015002

Abstract. We report on the realization of a compact atomic Mach–Zehnder-type Sagnac interferometer of 13.7 cm length, which covers an area of 19 mm^2 previously reported only for large thermal beam interferometers. According to Sagnac's formula, which holds for both light and atoms, the sensitivity for rotation rates increases linearly with the area enclosed by the interferometer. The use of cold atoms instead of thermal atoms enables miniaturization of Sagnac interferometers without sacrificing large areas. In comparison with thermal beams, slow atoms offer better matching of the initial beam velocity and the velocity with which the matter waves separate. In our case, the area is spanned by a cold atomic beam of 2.79 $m\,s^{-1}$, which is split, deflected and combined by driving a Raman transition between the two hyperfine ground states of ^{87}Rb in three spatially separated light zones. The use of cold atoms requires a precise angular alignment and high wave front quality of the three independent light zones over the cloud envelope. We present a procedure for mutually aligning the beam splitters at the microradian level by making use of the atom interferometer *itself* in different configurations. With this method, we currently achieve a sensitivity of 6.1×10^{-7} rad s^{-1} $Hz^{-1/2}$.

[1] Author to whom any correspondence should be addressed.

Contents

1. Introduction

The Sagnac phase [1] scales favourably for matter waves [2] in comparison with light interferometers. A large part of this advantage is compensated for by the brilliant sources and easy beam guidance solutions, which exist for light. The remaining difference is still sufficient to achieve high sensitivities with atom interferometers covering mm^2 or cm^2 scale areas for monitoring the Earth's rotation. Sensitivities comparable to square meter light interferometers [3] were impressively demonstrated with mm^2 Raman-type interferometers [4]. In this respect, miniaturized matter wave interferometers [5] have a high potential for high-resolution measurements for the Earth observation, which today is covered by large-scale light interferometers [6] or very-long-baseline interferometry. These two were compared in [7].

Key to reducing the dimensions of the atom light interferometer is the use of cold atoms, as in this case the velocity with which the two matter waves forming the interferometer arms separate scales with the photon recoil. For ^{87}Rb the recoil velocity is of the order of $cm\,s^{-1}$. In this paper, we report on a dual atom interferometer based on two counterpropagating intensive cold atomic beams, where the ratio of the velocities is about 230 compared to that for thermal beams of 4×10^4 [4]. An even better ratio of 47 was achieved in [5], where the beam splitting could be performed within a single laser beam leading to areas as large as $3.8\,mm^2$. In our case the large area was achieved by employing three spatially separated zones for the coherent manipulation by Raman processes. As shown in this paper, the three separated atom–light interaction zones have to be aligned to a few microradians in order to observe interference fringes. We have been inventing a procedure where different types of atom interferometers are sequentially employed for a perfect alignment at the position of the atoms. This scheme also allows for a measurement of the alignment stability. The coarse alignment is based on a symmetric Ramsey–Bordé interferometer [8, 9], which imposes less stringent requirements for the adjustment compared to the Mach–Zehnder-type interferometer [4, 5] that is employed for the final adjustment. In this paper, we will discuss the sensitivity to beam splitter alignment of the different interferometers and the alignment procedure of our Sagnac interferometer.

2. The experimental setup

Our cold atom gyroscope consists of two identical and simultaneously running ^{87}Rb atom interferometers with counterpropagating trajectories. The coherent beam splitting within the interferometry is realized by driving stimulated Raman transitions [10] between the magnetic

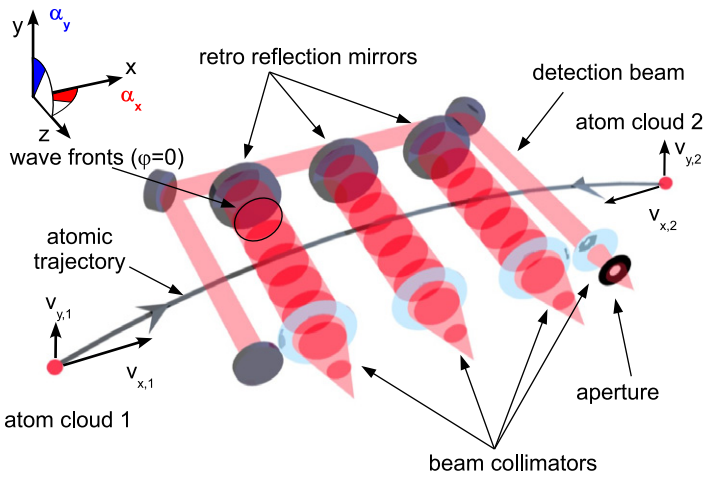

Figure 1. Schematic diagram of the compact large-area atomic Sagnac interferometer with atomic position vectors $\vec{x} = (x, y, z)$ and velocities $\vec{v} = (v_x, v_y, v_z)$. It consists of two interferometers with counterpropagating beams $v_{x,1} = -v_{x,2}$. Both have a small upward velocity component v_{y_i}. The atomic ensembles are simultaneously launched, coherently manipulated in the atom–light interaction zones *(big red beams)* and detected *(thin red beam)*. Each of the three atom light interaction zones features a motorized retro reflection mirror allowing for a remote-controlled alignment. The signal at the interferometer ports is measured by exciting the atoms with the detection beam and recording the fluorescence with a photo diode. With the aperture the diameter of the detection beam can be reduced. In this way, the width of the atomic velocity distribution contributing to the interference signal can be decreased mimicking effective lower ensemble temperatures.

insensitive hyperfine ground states $|5^2S_{1/2}, F = 1, m_F = 0\rangle$ and $|5^2S_{1/2}, F = 2, m_F = 0\rangle$, denoted by $|g\rangle$ and $|e\rangle$, respectively. These states are coupled via a two-photon process which is detuned by -728 MHz to the $|5^2P_{3/2}, F = 1\rangle$ state. A schematic diagram of our device is shown in figure 1. We will briefly recall the setup, while an extensive description can be found in [11, 12]. Each of the two sources comprises a two-dimensional magneto-optical trap (2D MOT) that forms a bright atomic beam from the background vapour to load a subsequent 3D MOT. The loading time of 300 ms at a rate of several 10^9 atoms s^{-1} allows for cycling rates of 2 Hz. By a moving molasses technique the atomic ensembles are launched with a forward drift velocity of 2.79 m s^{-1} and a fractional uncertainty of $< 3 \times 10^{-4}$.

After the launch, the atomic ensembles are prepared in the interferometer hyperfine ground state $|g\rangle$ comprising the following steps. First, atoms launched in the $|5^2S_{1/2}, F = 1\rangle$ states are transferred by optical pumping to the $|5^2S_{1/2}, F = 2\rangle$ states. Then, the magnetic sub-level degeneracy is lifted by a 600 mG bias field and a Raman π pulse transfers atoms from the excited interferometer state $|e\rangle$ to $|g\rangle$. Finally, the atoms remaining in the $|5^2S_{1/2}, F = 2\rangle$ states are pushed away by a beam resonant to the $|5^2S_{1/2}, F = 2\rangle \rightarrow |5^2P_{3/2}, F' = 3\rangle$ transition leaving the ensemble prepared in the $|g\rangle$ state. The light fields driving the Raman transitions are produced using a double 2 W high-power diode laser system. The differential frequency of 6.834 GHz

of the two emitted light fields is phase-locked on an ultra-stable microwave source, leading to a bandwidth of 6.2 MHz and a phase noise contribution of 2 mrad in the final interferometer. The two beams are superimposed and guided by three fibres to the spatially separated zones for the Raman manipulation. At the experiment they are collimated with a waist of 18.4 mm leading to beam splitter pulse durations of typically $\tau_{\pi/2} = 10\,\mu$s. The midpoint distance of two neighbouring light zones is 6.5 cm. In order to drive velocity selective Raman transitions with counterpropagating light fields, the three beams are retro reflected as in [4, 5, 12, 13]. The retro reflecting mirrors are remote controllable and aligned such that the optical axis of the light beams and the atomic trajectory enclose an angle of 87°. The resulting Doppler effect causes a large frequency shift relative to the frequency width of the Raman pulse and thereby lifts the degeneracy between the two possible momentum states [5, 12].

In order to read out the phase shift Φ of the interferometer, a state selective fluorescence detection [5, 12, 13] is performed. The number of atoms N_e in the upper state $|e\rangle$ is excited by a short light pulse of 800 μs driving the transition $|5^2S_{1/2}, F = 2\rangle \rightarrow |5^2P_{3/2}, F' = 3\rangle$. Subsequently, the atoms in the lower state $|g\rangle$ are transferred to $|e\rangle$ using optical pumping and repeated excitation of the atoms in the $|e\rangle$ state gives the total number of atoms $(N_g + N_e)$. We obtain the relative population as the output signal of each interferometer with $P = N_e/(N_g + N_e)$. The relative population of the two output ports of each interferometer depends on the phase shift Φ by

$$P(\Phi) = P_0 + A\cos(\Phi) \tag{1}$$

with an offset P_0 and an interference amplitude A leading to the contrast $C = A/P_0$. The detection is performed after a flight time of 116 ms when the atomic ensembles have a radius of about $\sigma_r = 5.2$ mm. In order to study the influence of a spatial selection of the detected atoms, a circular aperture of variable size is inserted into the detection light beam.

3. Criticality of the angular alignment for different interferometers

During each Raman-type interaction, the atoms sample a phase between the two light fields driving the transition. For the reported measurements, we have been employing two kinds of interferometers, namely the temporal Mach–Zehnder-type interferometer (figure 2(a)), based on the $\pi/2 - \pi - \pi/2$ sequence, and the temporal symmetric Ramsey–Bordé interferometer (figure 2(b)) realized by four $\pi/2$-pulses. The phase resulting from this sequence of Raman processes is given by

$$\Phi^{\mathrm{MZ}} = \phi_1(\vec{x}_1) - 2\phi_2(\vec{x}_2) + \phi_3(\vec{x}_3) \tag{2}$$

for the Mach–Zehnder configuration where $\vec{x}_i$ is the position of an atom at the ith Raman process in the light field. A constant rotation induces the phase shift $\Phi^{\mathrm{MZ}}_{\mathrm{rot}} = 2(\vec{k}_{\mathrm{eff}} \times \vec{v}) \cdot \vec{\Omega} T^2$ [1, 4, 5], where the effective wave vector $\vec{k}_{\mathrm{eff}} = \vec{k}_1 - \vec{k}_2$ is formed as a linear combination of the two superimposed light fields in the counter propagating configuration. For the sequence of a symmetric Ramsey–Bordé interferometer the phase dependence is given by

$$\Phi^{\mathrm{SRB}} = \phi_1(\vec{x}_1) - \phi_2(\vec{x}_2) - \phi_3(\vec{x}_3) + \phi_4(\vec{x}_4), \tag{3}$$

implying a response to rotations of $\Phi^{\mathrm{SRB}}_{\mathrm{rot}} = 2(\vec{k}_{\mathrm{eff}} \times \vec{v}) \cdot \vec{\Omega}(T^2 + TT_2)$ [1, 8, 9]. In both cases all other phase shifts were neglected. The first geometry offers the advantages of a higher scaling factor due to a larger enclosed area for a fixed total duration between the first and last beam

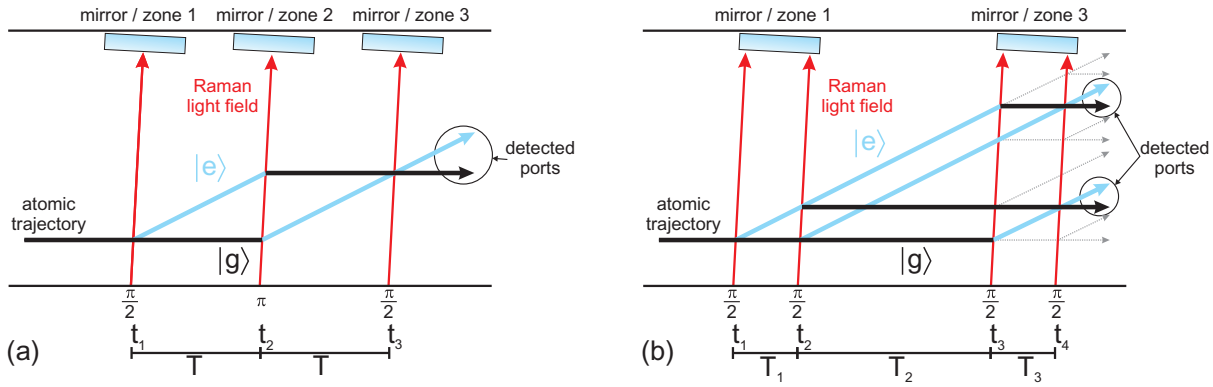

Figure 2. The sketches illustrate the two types of atom interferometers employed in the experiment for alignment and rotation sensing, the Mach–Zehnder-type and the symmetric Ramsey–Bordé interferometer. Figure (a) shows the well-known Mach-Zehnder-like interferometer realized by employing a sequence of three Raman pulses ($\pi/2 - \pi - \pi/2$) for splitting, deflecting and mixing the two interferometer arms featuring ideally a contrast of 100%. This interferometer is more alignment sensitive but spans a larger area. The symmetric Ramsey–Bordé interferometer (b) is generated by splitting the atomic ensemble four times with the help of Raman processes ($\pi/2$ pulse indicated by the red lines). Two interferometers (*solid black and blue line*), enclosing the same area, are formed with a maximum of 50% of the atoms. The other atoms contribute to the background (*dashed grey lines*). The delay between the first two and last two pulses, denoted by T_1 and T_3, are equal and called T in the following. The time in-between the two pairs of pulses is denoted by T_2. Due to the small splitting both interferometers are affected in a similar way by the wave front distortions across the atomic beam in transverse direction.

splitter pulses, and a potentially higher contrast as it does not feature incoherent output ports as inherited by the symmetric Ramsey–Bordé configuration. The latter geometry has a lower sensitivity to tilts of the beam splitting light fields as will be shown below.

The application of Gaussian-shaped light fields implies a spatial dependence of the Rabi frequency and of the imprinted phase over the interrogated atomic ensemble. The detection of the collective fluorescence averages over these effects, which causes a reduction of the fringe contrast. Moreover, imperfect parallel alignment of the three light fields driving the Raman transitions leads rapidly to decoherence due to the different phases accumulated over the different atomic trajectories (figure 3). For the considered small angular variations defined by the retro reflection mirrors, the contrast reducing contribution by the inhomogeneities of the Rabi frequencies hardly changes as confirmed both by the experiment and by numerical simulations. Hence, in the following considerations we will focus on the wave front effect resulting from the tiny angular effects and we write for the interference amplitude

$$A = \mathfrak{A}_{\mathrm{Rabi}}\mathfrak{A}_{\mathrm{WF}}. \tag{4}$$

The factor $\mathfrak{A}_{\mathrm{Rabi}}$ summarizes the influence of Rabi frequency inhomogeneities [14]. While $\mathfrak{A}_{\mathrm{Rabi}}$ is later fitted to the experimental data, it is now set to 1 for the following considerations.

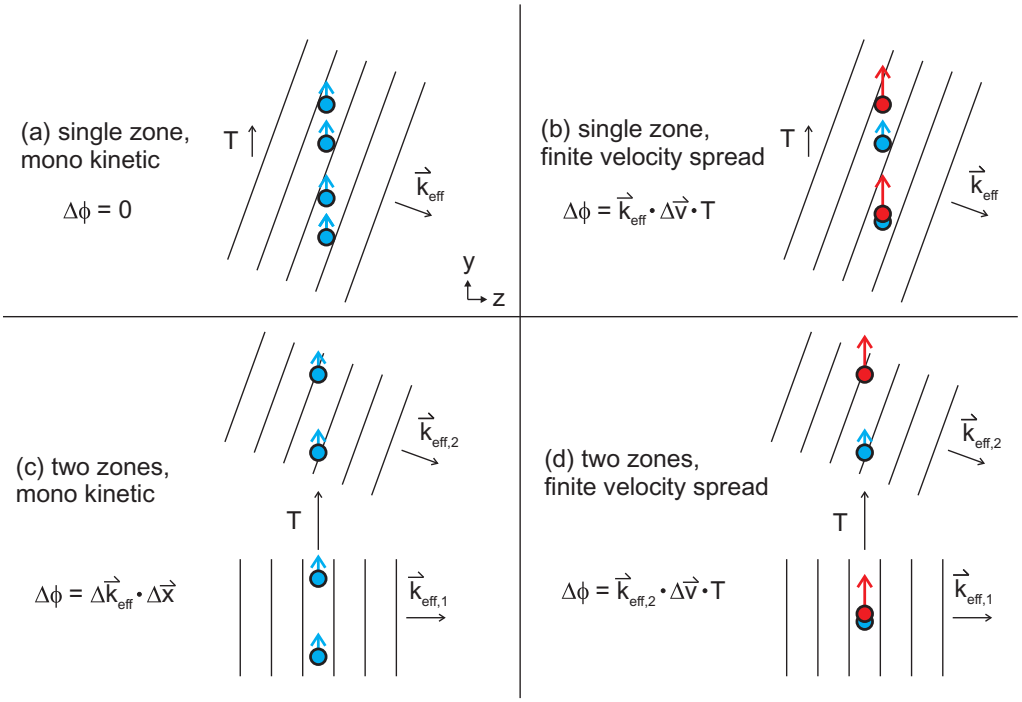

Figure 3. Schematic diagram visualizing the influence of the initial position and velocity of an atom on the phase sampled during two subsequent Raman pulses. We give the phase difference $\Delta\phi$ between two atoms with different starting conditions. Panels (a) and (b) depict the case when atoms travel between the first (or last) two Raman pulses in a symmetric Ramsey–Bordé interferometer. Panels (c) and (d) show the situation for the first and second (or second and third) Raman pulses in the Mach–Zehnder configuration. The main difference between the Ramsey–Bordé and the Mach–Zehnder interferometer is that in the first case the first (or last) two Raman pulses are implemented within the same light field. Panel (a) depicts the case of two atoms (blue dots on the left side) with different starting positions but identical velocities travelling to the top. Panel (b) depicts the situation of identical starting positions but different velocities (blue and red dot). The same applies to panels (c) and (d) for the Mach–Zehnder topology with two spatially separated light fields. $\Delta\vec{x}$ and $\Delta\vec{v}$ denote the spatial distance and the velocity difference between the two atoms, respectively, and $\Delta\vec{k}_{\mathrm{eff}}$ is given by the difference between the two wave vectors $\vec{k}_{\mathrm{eff},1}$ and $\vec{k}_{\mathrm{eff},2}$ in the spatially separated zones.

$\mathfrak{A}_{\mathrm{WF}}$ describes the wave front influences on contrast, dominated by the relative tilt of the three spatially separated effective wave fronts. The cold atomic ensembles propagate in both the x- and y-direction (see figure 1), but in the following discussion we will focus on motion in the y-direction. The light beams driving the Raman transitions are propagating nearly along the z-direction with a small angular offset with respect to the x- and y-axis. In order to calculate this reduction of the fringe amplitude the multi-particle interferometer signal can be written by

averaging over all trajectories, which is

$$P_{\text{total}} = \int_{-\infty}^{\infty} f(y) \cdot g(v_y) \cdot P(\Phi(y, v_y))\, \mathrm{d}y\, \mathrm{d}v_y. \tag{5}$$

For simplicity reasons, only the vertical direction with initial position y and velocity v_y of the atom at $t = 0$ is taken into account. Nevertheless, it can be shown that for all the remaining coordinates this calculation can be performed separately. $P(\Phi(y, v_y))$ is the interference signal of the form of (1). The other factors, $f(y) = ((2\pi)^{1/2}\sigma_r)^{-1} \exp\left(\frac{-(y-y_0)^2}{2\sigma_y^2}\right)$ and $g(v_y) = ((2\pi)^{1/2}\sigma_{v_y})^{-1} \exp\left(\frac{-(v_y-v_{y,0})^2}{2\sigma_{v_y}^2}\right)$, represent the 1D normal distributions for space and velocity regarding the ensemble's initial dimensions and temperature equivalent with, in our experiment, $\sigma_y = 3.8\,\text{mm}$ and $\sigma_{v_y} = \sqrt{k_B \Theta_y / m} = 0.031\,\text{m}\,\text{s}^{-1}$ as standard deviations. Here, k_B is the Boltzmann constant, $v_{y,0}$ is the initial average velocity of the cloud in the y-direction at $t = 0$, y_0 the centre of mass position at $t = 0$, $\Theta_y = 10\,\mu\text{K}$ is the temperature equivalent in the vertical direction of the beam splitting light fields and m is the atomic mass of ^{87}Rb.

The phase $\phi_{\alpha_{y,i}}(y, v_y)$ seen by a single atom during one beam splitter pulse in the case of a tilted wave front is given by

$$\begin{aligned}\phi_{\alpha_{y,i}}(y, v_y) &= k_{\text{eff}} \left[\left(a_i - y - v_y t_i + \tfrac{1}{2} g t_i^2\right) \sin(\alpha_{y,i})\right] \\ &\approx k_{\text{eff}} \left[\left(a_i - y - v_y t_i + \tfrac{1}{2} g t_i^2\right) \alpha_{y,i}\right].\end{aligned} \tag{6}$$

Here, t_i is the time of the ith beam splitter pulse, a_i represents the coordinate of the rotation axis of the corresponding retro reflection mirror, $\alpha_{y,i}$ is its tilting angle with respect to z in the chosen laboratory reference frame and g is the local gravitational acceleration in which higher-order inertial phase shifts (see e.g. [15]) are neglected. For small angles $\alpha_{y,i}$ the sine function can be approximated by its first order.

Adding up the phases (6) according to the rule (2) and inserting the result into (5) gives the following solution for a Mach–Zehnder-type interferometer signal

$$P_{\text{total}}^{\text{MZ}} = P_0^{\text{MZ}} + \mathfrak{A}_{\text{WF}}^{\text{MZ}} \cos(\Phi_0^{\text{MZ}}),$$

with

$$\mathfrak{A}_{\text{WF}}^{\text{MZ}} = \frac{1}{2} \exp\left(-\frac{\left[k_{\text{eff}}\sigma_y \left(\Delta_{1,2} - \Delta_{2,3}\right)\right]^2}{2}\right) \exp\left(-\frac{\left[k_{\text{eff}}\sigma_{v_y} \left(t_1(\Delta_{1,2} - \Delta_{2,3}) - 2T\,\Delta_{2,3}\right)\right]^2}{2}\right), \tag{7}$$

$$\begin{aligned}\Phi_0^{\text{MZ}} = k_{\text{eff}}[&(a_1 - y_0 - v_{y,0}t_1 + \tfrac{1}{2} g t_1^2)\alpha_{y,1} - 2(a_2 - y_0 - v_{y,0}t_2 + \tfrac{1}{2} g t_2^2)\alpha_{y,2} \\ &+ (a_3 - y_0 - v_{y,0}t_3 + \tfrac{1}{2} g t_3^2)\alpha_{y,3}]\end{aligned} \tag{8}$$

and

$$\Delta_{i,j} = \alpha_{y,i} - \alpha_{y,j}.$$

From this result it becomes apparent that the fringe amplitude $\mathfrak{A}_{\text{WF}}^{\text{MZ}}$ averaged over the ensemble is influenced by the spatial width and velocity distribution of the atomic cloud (see figures 3(c) and (d)) as well as by the time between the beam splitter pulses if the wave vectors are not parallel. In order to lower the sensitivity to misalignments of the beam splitters, it is

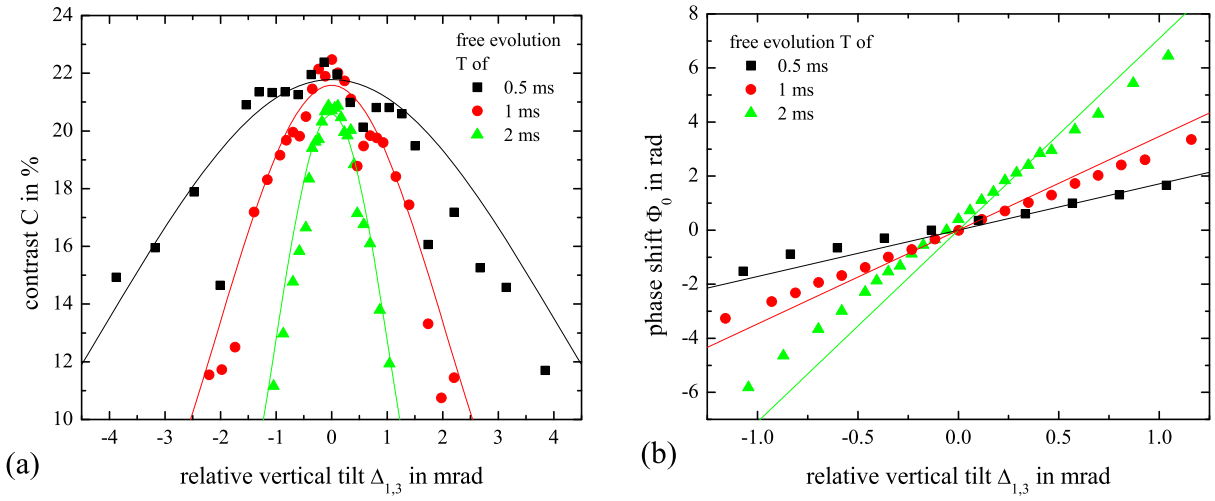

Figure 4. The graphs show the dependence of contrast and phase offset on relative beam splitter tilts in a symmetric Ramsey–Bordé configuration. Both diagrams include the measured values (symbols) and the theoretical model (lines). The reduced contrast (a) and phase offset (b) as a function of the vertical tilt difference $\Delta_{1,3}$ is depicted for different pulse delays $T = T_1 = T_3$ (see figure 2). The contrast reduction factor due to Rabi inhomogeneities $\mathfrak{A}_{\mathrm{Rabi}}$ was taken by fitting the curves neglecting higher order wave front contributions. The slight disagreement in measured and calculated phase shifts arises as a crosstalk to the horizontal axis occurs when tilting the mirrors in the vertical direction.

advantageous to choose the symmetric Ramsey–Bordé geometry with only two interaction zones. Performing the same calculation as above for the new geometry results in

$$\mathfrak{A}_{\mathrm{WF}}^{\mathrm{SRB}} = \frac{1}{4}\exp\left(-\frac{\left[k_{\mathrm{eff}} T \sigma_{v_y} \Delta_{1,3}\right]^2}{2}\right) \tag{9}$$

and

$$\Phi_0^{\mathrm{SRB}} = k_{\mathrm{eff}}\left[-v_{y,0} T \Delta_{1,3} - \frac{g}{2}\left((t_1^2 - t_2^2)\alpha_{y,1} - (t_3^2 - t_4^2)\alpha_{y,3}\right)\right]. \tag{10}$$

In this case, the contrast reduction is not attributed to the spatial distribution of the ensemble any more, which is illustrated in figures 3(a) and (b). Moreover, in the symmetric Ramsey–Bordé geometry the critical time with which the exponential decay of the amplitude scales is determined by the pulse delay between the first two and last two $\pi/2$ pulses. This time is much shorter than the travel time of the atoms required for covering the distance between the three interaction zones of the Mach–Zehnder interferometer.

To verify the presented model, we measured the contrast in the symmetric Ramsey–Bordé geometry as well as the phase offset in dependence of the tilt difference of the two retro reflecting mirrors. As shown in figure 4, we find good agreement of the measured contrast to (9). Adapting the fringe amplitude from (9) to the measured contrast values, we find a tilt-independent contrast reduction factor $\mathfrak{A}_{\mathrm{Rabi}} \approx 0.42$ and an atomic temperature equivalent of $\Theta_y = 10\,\mu\mathrm{K}$ can be confirmed. The mismatch between the measured phase offset (figure 4(b)) and (10) can be attributed to a crosstalk between the horizontal and vertical directions when

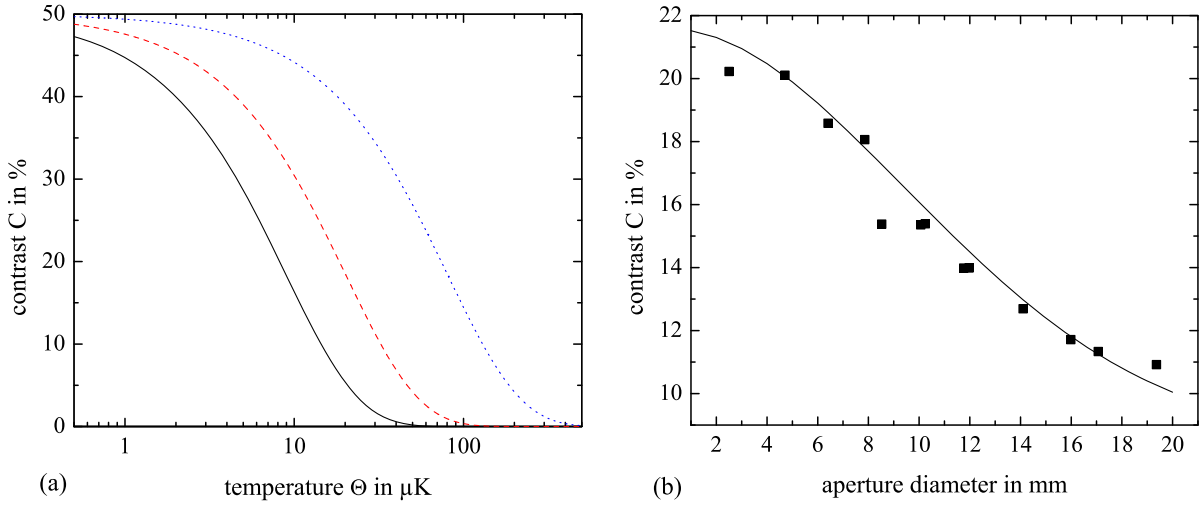

Figure 5. The calculated (a) and measured (b) contrast of a symmetric Ramsey–Bordé interferometer for different effective atomic cloud diameters. This experiment was performed by varying the diameter of the detection beam. For reduced beam diameters, only a fraction of the atoms, spread out over a smaller area across the light fields, contributes to the signal. This has a similar effect on averaging as operating the interferometer with ensembles cooled to lower temperatures as assumed in our theoretical model. The calculations were performed for various tilts $\Delta_{1,3}$ between the two spatially separated light fields driving the Raman transitions, i.e. mirror 1 and mirror 3 (black -1.5 mrad, red dotted -1 mrad, blue dotted -0.5 mrad). The measurements (symbols) shown in (b) were carried out with an angular mismatch of 1.5 mrad. The line denotes the numerical simulation including also Rabi frequency inhomogeneities.

tilting the mirror. This leads to an additional phase shift observed by the experiment. Also, the dependence of the contrast on time T found in (9) can be shown in the experiment (see figure 4(a)). In figure 5(a), the correlation between the ensemble's temperature equivalent and the signal contrast is shown for different tilting angles.

Since the temperature of the atomic cloud cannot be tuned easily in the experiment, we vary the integration area during detection by inserting an aperture of variable diameter into the light beam used for fluorescence detection (see figure 1). This leads to two effects. Firstly, one averages over a smaller volume of the atomic cloud and hence the influence of the spatial Gaussian inhomogeneity of the Rabi frequency is reduced. Secondly, the velocity spread transverse to the Raman beams is narrowed as higher velocity classes are excluded from the detection process. This reduces the phase dispersion due to wave front tilts. The values for the measured and numerically simulated contrast are shown in figure 5(b) for a relative mirror tilt of $\Delta_{1,3} = 1.5$ mrad, regarding also Rabi frequency inhomogeneities in the numerical simulation. The contrast increases as the diameter of the aperture is reduced, as expected. This is equivalent to reducing the expansion rate and the initial size of the atomic cloud, as can be done in a matter wave guide demonstrated, for example, in [16, 17].

Based on (7), we can deduce the demand for the alignment of the relative pointing of the beam splitter light fields. Using three separated beam splitter zones with a time $T = 24.7$ ms,

we obtain a $1/\sqrt{e}$-radius of 13 μrad for the fringe amplitude in dependence of the tilting angle $\Delta_{2,3}$. The alignment accuracy of the retro reflecting mirrors has to match this demand in order to obtain an interferometer signal.

The described model and its confirmation with experimental studies provide us with a good understanding of the impact of wave front tilts and give the necessary tools for the alignment of spatially separated beam splitter light fields in atom interferometers.

4. Beam splitter alignment recipe

Based on the described model, we present in this section the procedure for the angular alignment of the three spatially separated light fields for driving the Raman transitions in the final Mach–Zehnder interferometer. The recipe comprises two steps: a pre-adjustment with respect to local gravity and the coarse and fine adjustment by the atom interferometer itself.

First, the central mirror for reflecting the π pulse of the Mach–Zehnder interferometer is aligned perpendicularly to gravity. For the horizontal pre-adjustment the light fields are not perfectly orthogonal to the atomic trajectory but slightly tilted by an angle of $\alpha_D = 3^\circ$, which is necessary to ensure the Doppler selection in the described beam splitter configuration (see above). By using a penta prism and the reflection of the redirected light field on a water surface, we can adjust the beam splitter light field in the vertical direction, leading to a coarse adjustment perpendicular to the Earth acceleration $\vec{g}$ with an accuracy of a few mrad. As a criterion for the perfect overlap of the incoming and the retro reflected beam, we use the coupling into the fibres, which guide the laser beams to the interferometer. Then, a reference mirror extending over all the three interaction zones is implemented for the next alignment steps. The large mirror with a reflective surface of $170 \times 40\,\mathrm{mm}^2$ and a planarity of $\lambda/20$ serves as a reference for aligning the light beams driving the $\pi/2$ pulses in the final Mach–Zehnder geometry. Finally, the reference mirror is replaced by three single mirrors. With this pre-adjustment the beam splitter light fields have a relative pointing accuracy of about 1 mrad in both the axes.

A more precise alignment in the horizontal direction can be performed by scanning over the Raman resonance separately with each of the three light fields driving a π pulse. For the scan, the frequency difference of the two counterpropagating beams is varied. In this Doppler-sensitive configuration, the resonance frequency is shifted, due to the tilt in the horizontal direction by the angle α_D. Depending on the length of the pulse, which determines the resolution of the resonance and which is for this purpose 60 μs in our case, α_D in the three cases can be optimized to a relative accuracy of 0.1 mrad.

Based on this pre-adjustment we still obtain vanishing contrast in the Mach–Zehnder atom interferometer configuration extended over all three interaction zones. This is due to the high demand in the relative beam splitter wave front alignment of better than 13 μrad as described above. Nevertheless, the pre-adjustment is sufficient for the realization of a four-pulse atom interferometer configuration, comprising two interaction zones and hence two mirrors.

At this point, the alignment with improved accuracy can be continued with the atom interferometer *itself*. The two symmetric Ramsey–Bordé interferometers are used to independently adjust the first and the third mirror with respect to the central mirror. For this purpose, the first pair of $\pi/2$ pulses is applied at the central mirror and the second pair at the third mirror for the interferometer operating with the cold ensemble travelling from the left (see figure 6(a)). Maximizing the contrast by changing the tilts of the third mirror with respect to the central mirror results in better alignment. This is repeated while one increases stepwise the

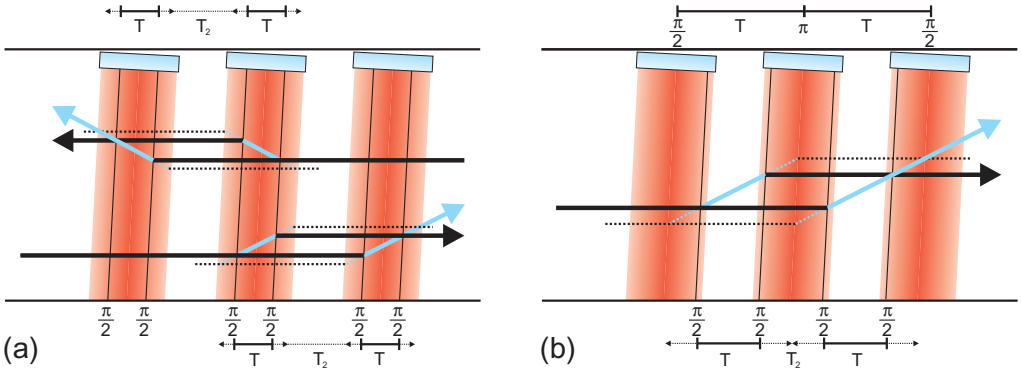

Figure 6. Interferometer configurations used for coarse and fine alignment. Raman light fields are illustrated by the red-coloured area and the atomic trajectories are represented by black and light blue arrows. In these pictures the interferometric alignment procedure is illustrated. With the symmetric Ramsey–Bordé interferometer (a), which is at first spread over two beam splitter zones (central and outer mirrors), the outer mirror can be aligned with respect to the central one by optimizing the contrast. This procedure is repeated for increasing T (dotted). The maximum pulse delay T is limited by the spatial extension of the light field. Then the mirrors are sufficiently well aligned that the Ramsey–Bordé interferometer can be extended by using all three beam splitter zones (b). The final step is the transformation from this extended Ramsey–Bordé into a large three-pulse atom interferometer (dotted) by again stepwise maximizing the contrast for increasing T.

sensitivity to the angular alignment by increasing the pulse delay T from 100 μs up to 8 ms. For the other mirror, the alignment is performed analogously to the atoms travelling from the right.

After this procedure the mutual alignment of the mirror is sufficient to extend each of the interferometers over all three interaction zones. At this point, the first $\pi/2$ pulse splits the atomic ensemble at the first mirror and the second and the third $\pi/2$ pulse is applied to the atoms while they pass through the central mirror. The fourth $\pi/2$ pulse is exerted at the third mirror (see figure 6(b)). Stepwise alignment of the two outer mirrors while the time T is extended leads to an interferometer very close to the final Mach–Zehnder topology. After enlarging the time T up to 24.7 ms, we end up with our final three-pulse atom interferometer, enclosing the large area of 19 mm^2.

With this method, a relative pointing alignment at the μrad level is achieved by resolving a fringe pattern as shown in figure 7. Both signal amplitudes are almost equal with contrasts of 18.2 and 18.7%. From midfringe operation a sensitivity of 6.1×10^{-7} rad s^{-1} Hz$^{-1/2}$ is obtained. Thus, a full systematic analysis as shown in [5], which is yet to be performed, would allow for a measurement of the Earth's rotation rate with a relative precision of 10^{-2} in 1 s. The resolution results from the scaling factor, i.e. the enclosed area, the contrast and the signal-to-noise ratio. We assume that the observed contrast is only partially a result of the residual mismatch of the angular alignment. Temporal Mach–Zehnder-type interferometers extended only over one of the spatially separated Raman interaction zones, which resembles very much a configuration of the experiments reported by Landragin [5], feature a contrast of

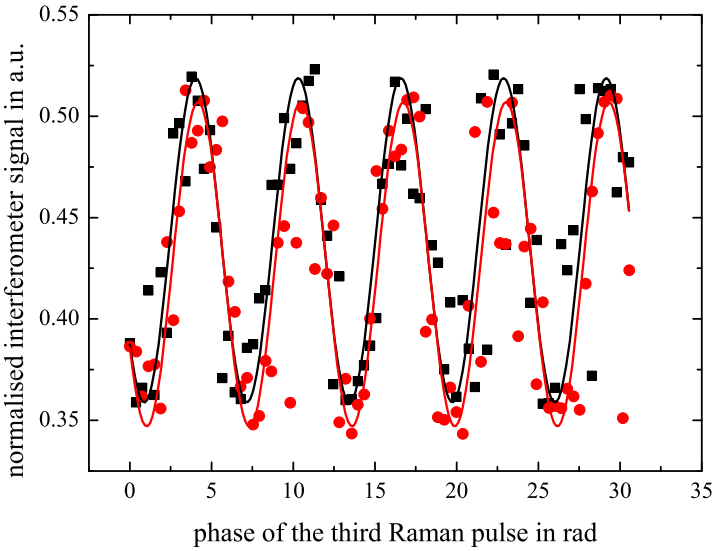

Figure 7. Fringe pattern of the two large counter propagating Sagnac interferometers (red and black dots) requiring an alignment of the Raman-type beam splitters at the microradian level. The interrogation time is extended to $T = 24.7$ ms, enabling an area as large as 19 mm^2. The fringe pattern is obtained by repeating the interferometer cycle while the phase of the two Raman lasers is altered before the third beam splitter pulse.

30% at $T = 3$ ms. Our experimental analysis combined with our theoretical model indicates that the initial source temperature and imperfect state preparation are the main reasons for the observed contrast. The signal-to-noise ratio of the sensor is 30. This results mainly from the rotation noise of the platform, which we estimate to lead to a signal-to-noise ratio of about 34, and from instrumental noise induced by the Raman process. The signal-to-noise ratio of the detection system is 210 and, hence, is currently not limiting the performance.

5. Conclusion

In this work, we realized a Sagnac sensor with matter waves. Rotation rates are encoded in the differential phase shift between two spatially overlapping interferometers operated with counterpropagating beams of cold atoms. The two Mach–Zehnder-like interferometers feature three spatially separated interaction zones, where the beams are split, deflected and recombined by driving Raman transitions between the hyperfine states of ^{87}Rb. The interferometers have a length of only 13.7 cm and enclose an area of 19 mm^2 similar to what was previously achieved for a large interferometer based on thermal atomic beams [4]. The use of cold and slow atomic beams allows for better matching of the speed of the atomic beam to the velocity with which the two interferometer arms separate. However, in implementing cold atom interferometry with spatially separated light zones, one faces the difficulty of stringent requirements with respect to the parallel alignment of the light beams driving the Raman transitions. This results from the fact that in an interferometer operated with slow atoms, the beam divergence, which is determined by the atomic temperature, is large compared to fast thermal beams of a similar vertical temperature equivalent. We developed a model to quantify the effect and calculate the influence of these

misalignments for a symmetric Ramsey–Bordé interferometer, and inferred from this model the more stringent demands of the Mach–Zehnder-type interferometer in this respect. Based on this model, we have developed a recipe for aligning the atom interferometer. This process employs a symmetric Ramsey–Bordé interferometer, which is transformed in a stepwise process into a Mach–Zehnder-type interferometer with $T = 24.7$ ms by aligning the pointing angle of light fields at a microradian level with respect to each other. In this way, we could enhance the area by a factor of 6.3 with respect to the symmetric Ramsey–Bordé interferometer with $T = 2$ ms. The contrast for the two interferometers is 18.2 and 18.7%. With this setup we achieve a resolution for rotation rates of 6.1×10^{-7} rad s^{-1} Hz$^{-1/2}$. Key to a better performance is to lower the temperature of the atomic ensemble and to improve the state preparation with respect to parasitic spontaneous emission processes. Combined with a better inertial isolation this should allow for venturing in the 10^{-8} rad s^{-1} Hz$^{-1/2}$ regime. Applying techniques such as double diffraction [18] combined with a multi-photon transfer technique [19–23] should provide a means to further enhance the scale factor. This will lead to an improvement of the short-term sensitivity by at least one order of magnitude.

Acknowledgments

This work was supported in part by the Deutsche Forschungsgemeinschaft (SFB407) and in part by the European Union (contract no. 012986-2 (NEST), FINAQS, Euroquasar, IQS). We also thank the Centre for Quantum Engineering and Space Time Research QUEST. MG and GT thank the Max-Planck-Gesellschaft for financial support. GT also thanks the INTERCAN network and the UFA-DFH for financial support.

References

[1] Sagnac G 1913 *C. R. Acad. Sci., Paris* **157** 708
[2] Berman P (ed) 1997 *Atom Interferometry* (San Diego, CA: Academic)
[3] Schreiber U, Schneider M, Rowe C H, Stedman G E, Cooper S J, Schlüter W and Seeger H 2000 *Phys. Chem. Earth* A **25** 805
[4] Gustavson T, Bouyer P and Kasevich M 1997 *Phys. Rev. Lett.* **78** 2046
[5] Gauguet A, Canuel B, Lévèque T, Chaibi W and Landragin A 2009 *Phys. Rev.* A **80** 063604
[6] Schreiber K, Klügel T, Velikoseltsev A, Schlüter W, Stedman G and Wells J-P 2009 *Pure Appl. Geophys.* **166** 1485
[7] Mendes Cerveira P, Böhm J, Schuh H, Klügel T, Velikoseltsev A, Schreiber K and Brzezinski A 2009 *Pure Appl. Geophys.* **166** 1499
[8] Bordé C 1989 *Phys. Lett.* A **140** 126
[9] Riehle F, Kisters T, Witte A, Helmcke J and Bordé C 1991 *Phys. Rev. Lett.* **67** 177
[10] Kasevich M and Chu S 1991 *Phys. Rev. Lett.* **67** 181
[11] Müller T, Wendrich T, Gilowski M, Jentsch C, Rasel E and Ertmer W 2007 *Phys. Rev.* A **76** 63611
[12] Müller T, Gilowski M, Zaiser M, Berg P, Schubert C, Wendrich T, Ertmer W and Rasel E 2009 *Eur. Phys. J.* D **53** 273
[13] Peters A, Chung K and Chu S 1999 *Nature* **400** 849
[14] Kasevich M, Weiss D, Riis E, Moler K, Kasapi S and Chu S 1991 *Phys. Rev. Lett.* **66** 2297
[15] Bongs K, Launay R and Kasevich M 2006 *Appl. Phys.* B **84** 599
[16] Wang Y-J, Anderson D, Bright V, Cornell E, Quentin D, Kishimoto T, Prentiss M, Saravanan R, Segal S and Wu S 2005 *Phys. Rev. Lett.* **94** 090405

[17] Wu S, Su E and Prentiss M 2007 *Phys. Rev. Lett.* **99** 173201
[18] Lévèque T, Gauguet A, Michaud F, Pereira Dos Santos F and Landragin A 2009 *Phys. Rev. Lett.* **103** 080405
[19] McGuirk J, Snadden M and Kasevich M 2000 *Phys. Rev. Lett.* **85** 4498
[20] Müller H, Chiow S, Long Q, Herrmann S and Chu S 2008 *Phys. Rev. Lett.* **100** 180405
[21] Chiow S-W, Herrmann S, Chu S and Müller H 2009 *Phys. Rev. Lett.* **103** 050402
[22] Cladé P, Guellati-Khélifa S, Nez F and Biraben F 2009 *Phys. Rev. Lett.* **102** 240402
[23] Bouchendira R, Cladé P, Guellati-Khélifa S, Nez F and Biraben F 2011 *Phys. Rev. Lett.* **106** 080801